A nanosecond time-resolved XFEL analysis of structural changes associated with CO release from cytochrome c oxidase

Shimada, Atsuhiro ; Kubo, Minoru ; Baba, Seiki ; Yamashita, Keitaro ; Hirata, Kunio ; Ueno, Go ; Nomura, Takashi ; Kimura, Tetsunari ;…

(Citation)
Science Advances,3(7):e1603042-e1603042

(Issue Date)
2017-07

(Resource Type)
journal article

(Version)
Version of Record

BIOCHEMISTRY

A nanosecond time-resolved XFEL analysis of structural changes associated with CO release from cytochrome c oxidase

Atsuhiro Shimada,[1]* Minoru Kubo,[2,3]* Seiki Baba,[4]* Keitaro Yamashita,[2] Kunio Hirata,[2,3] Go Ueno,[2] Takashi Nomura,[2] Tetsunari Kimura,[5] Kyoko Shinzawa-Itoh,[1] Junpei Baba,[1] Keita Hatano,[1] Yuki Eto,[1] Akari Miyamoto,[1] Hironori Murakami,[4] Takashi Kumasaka,[4] Shigeki Owada,[2] Kensuke Tono,[4] Makina Yabashi,[4] Yoshihiro Yamaguchi,[6] Sachiko Yanagisawa,[6] Miyuki Sakaguchi,[6] Takashi Ogura,[6] Ryo Komiya,[7] Jiwang Yan,[7] Eiki Yamashita,[8] Masaki Yamamoto,[2] Hideo Ago,[2†] Shinya Yoshikawa,[1†] Tomitake Tsukihara[1,8,9†]

Bovine cytochrome c oxidase (CcO), a 420-kDa membrane protein, pumps protons using electrostatic repulsion between protons transferred through a water channel and net positive charges created by oxidation of heme *a* (Fe_a) for reduction of O_2 at heme a_3 (Fe_{a3}). For this process to function properly, timing is essential: The channel must be closed after collection of the protons to be pumped and before Fe_a oxidation. If the channel were to remain open, spontaneous backflow of the collected protons would occur. For elucidation of the channel closure mechanism, the opening of the channel, which occurs upon release of CO from CcO, is investigated by newly developed time-resolved x-ray free-electron laser and infrared techniques with nanosecond time resolution. The opening process indicates that Cu_B senses completion of proton collection and binds O_2 before binding to Fe_{a3} to close the water channel using a conformational relay system, which includes Cu_B, heme a_3, and a transmembrane helix, to block backflow of the collected protons.

INTRODUCTION

Cytochrome c oxidase (CcO) is the terminal oxidase of cellular respiration, which reduces O_2 coupled with a proton pumping process. Bovine CcO is a large transmembrane protein, which is a 420-kDa dimer in the crystalline state (Fig. 1A). Each monomer includes four redox active metal sites [heme *a* (Fe_a), heme a_3 (Fe_{a3}), Cu_B, and Cu_A]. The O_2 reduction site contains Cu_B and Fe_{a3} (Fig. 1B). O_2 is transiently trapped at Cu_B before binding to Fe_{a3} (*1*–*3*). To O_2 at Fe_{a3} (not to O_2 at Cu_B), four electrons are sequentially transferred from cytochrome c on the P-side via Cu_A and Fe_a, and four protons are transferred from the N-side (the P- and N-sides designate the outside and inside of the mitochondrial inner membrane, which are positively and negatively charged in the cell, respectively). In addition, protons used for pumping are actively transferred through the H-pathway, which is composed of a water channel and a hydrogen bond network operating in tandem (Fig. 1B). The hydrogen bond network is connected to a proton storage site via a short hydrogen bond network (Fig. 1B). The water channel in the H-pathway includes water cavities (Fig. 1C). Each cavity contains at least one mobile water molecule, whereas the rest of the water channel allows transfer of water molecules driven by thermal motion of the protein moiety. Thus, the water cavities promote overall efficiency in proton transfer and water molecule exchange through the water channel because the mobile water molecules in the cavities accelerate water exchange and thus proton transfer. The elimination of the cavity efficiently decreases water (hydronium ion) exchange to block backward flow of protons from the hydrogen bond network at least on the physiologically relevant time scale.

The protons for pumping are transferred to the hydrogen bond network through the water channel from the N-side as hydronium ions. Heme *a* is located close to the hydrogen bond network (Fig. 1B) (*1*–*3*). The driving force for the proton pumping process is provided by electrostatic repulsion between the protons transferred from the N-side to the hydrogen bond network and the net positive charges created upon transfer of electrons from Fe_a^{2+} to the O_2 reduction site. The directionality of the electrostatic repulsion process is induced by closure of the water channel by the formation of a bulge at S382 in a transmembrane helix (helix X), which eliminates the largest cavity located near the upper end of the water channel (Fig. 1C). Extensive x-ray structure analyses of various oxidation and ligand binding states have indicated that the largest cavity is detectable only in the ligand-free fully reduced state and that O_2 binding to Fe_{a3} as well as elevation of the oxidation state of Fe_{a3}^{2+} eliminate this cavity by the bulge formation at S382 (Fig. 1C) (*4*). Thus, there are two different structural species relating to the state of the water channel. The species with the largest cavity is designated as the "open structure," and the species without the largest cavity is designated as the "closed structure" (Fig. 1C) (*2*, *4*). (The diversity in the proton pumping mechanism of CcO among organisms is described in text S1.)

It is necessary to close the water channel before oxidation of heme *a*, which is triggered by O_2 binding to Fe_{a3}. This is because binding of O_2 to Fe_{a3} triggers oxidation of heme *a*, which repels the protons to be pumped without directionality, if the water channel is not closed. Furthermore, because the water channel is open only in the ligand-free fully reduced state as described above (*4*), in each catalytic cycle, four protons to be

[1]Picobiology Institute, Graduate School of Life Science, University of Hyogo, 3-2-1 Kouto, Kamigori-cho, Ako-gun, Hyogo 678-1297, Japan. [2]RIKEN SPring-8 Center, 1-1-1 Kouto, Sayo-cho, Sayo-gun, Hyogo 679-5148, Japan. [3]Japan Science and Technology Agency, Precursory Research for Embryonic Science and Technology (PRESTO), 4-1-8 Honcho, Kawaguchi, Saitama 332-0012, Japan. [4]Japan Synchrotron Radiation Research Institute, 1-1-1, Kouto, Sayo-cho, Sayo-gun, Hyogo 679-5198, Japan. [5]Graduate School of Science, Kobe University, 1-1 Rokkodai, Nada, Kobe, Hyogo 657-8501, Japan. [6]Picobiology Institute, Graduate School of Life Science, University of Hyogo, 1-1-1 Kouto, Sayo, Hyogo 679-5148, Japan. [7]Department of Mechanical Engineering, Keio University, 3-14-1 Hiyoshi, Kohoku-ku, Yokohama 223-8522, Japan. [8]Institute for Protein Research, Osaka University, 3-2 Yamadaoka, Suita, Osaka 565-0871, Japan. [9]Japan Science and Technology Agency, Core Research for Evolutional Science and Technology (CREST), 4-1-8 Honcho, Kawaguchi, Saitama 332-0012, Japan.
*These authors contributed equally to this work.
†Corresponding author. Email: tsuki@protein.osaka-u.ac.jp (T.T.); yoshi@sci.u-hyogo.ac.jp (S.Y.); ago@spring8.or.jp (H.A.)

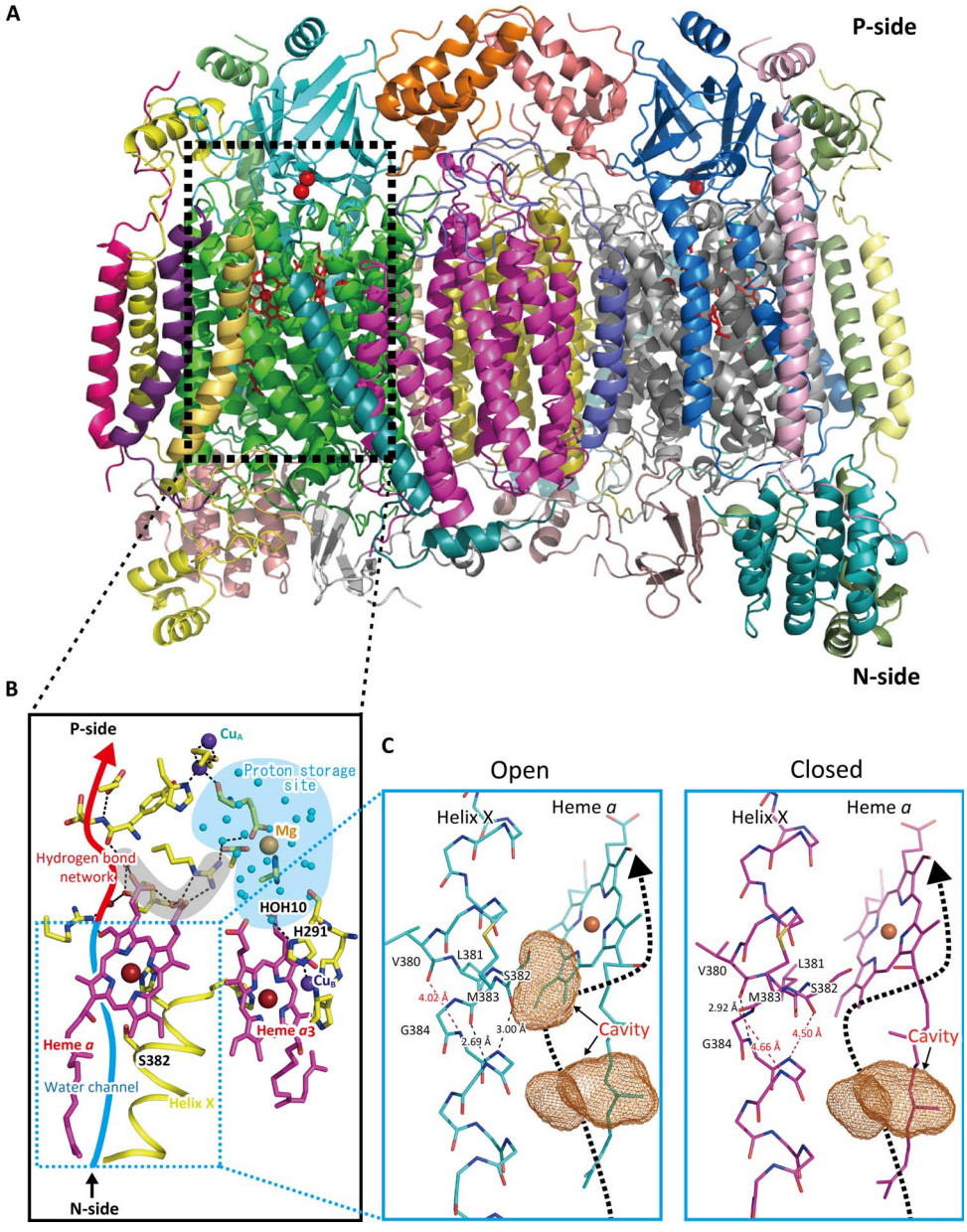

Fig. 1. The structure of the H-pathway. (**A**) Location of the H-pathway in the x-ray structure of bovine heart CcO, which is dimeric in the crystalline state (*1*). (**B**) Structure of the H-pathway. The location of the water channel and the location of the hydrogen-bond network are indicated by the blue and red curves. The short hydrogen bond network (indicated by the gray area) connects the hydrogen bond network of the H-pathway and the proton storage site (the blue area). Water molecule HOH10 in the proton storage site forms a hydrogen bond to H291. (**C**) Structure of the water channel. Helix X structures of the closed structure with two bulges at S382 and M383 and the open structure with one bulge at V380 are shown in the right and left panels. These bulges are indicated with red dotted lines. Water cavities represented by the brown cages were calculated with a probe radius of 1.2 Å using the VOIDOO program (*34*). The broken arrows indicate the location of the water channel, which includes the water cavities (brown cages). The channel extends up to R38, which is located on the N-side end of the hydrogen bond network of the H-pathway, where it is hydrogen-bonded to the formyl group of heme *a*.

pumped must be collected in the proton storage site of the hydrogen bond network between attainment of the ligand-free fully reduced state and binding of O_2 to Fe_{a3} (*4*, *5*). Closure of the water channel after collection of these four protons and before heme *a* oxidation is critical for effective proton pumping (that is, for attaining $H^+/e^- = 1$) (*1*). The mechanism for facilitating timely closure of this water channel is one of the most fundamental bioenergetics subjects to be elucidated.

In order to investigate the channel closure mechanism, newly developed time-resolved XFEL [serial femtosecond rotational crystallography (SF-ROX) method (*6*) using many large single crystals] and infrared (IR) techniques with the pump-probe method were applied to examine the CO release process from CcO upon photolysis. Carbon monoxide (CO) binds readily to Fe^{2+}-porphyrins (but not to Fe^{3+}-porphyrins) to form complexes that have quite distinctive spectral properties of both the heme and the bound CO. Because it is reasonable to assume that CO competes with O_2 for a common binding site, a better understanding of CO binding is expected to provide insight into O_2 binding. Thus, CO has been widely used as a probe of the active site

of heme proteins. Beginning with the classical studies of Warburg *et al.* [as presented in the study of Yoshikawa and Shimada (*1*)], which led to the discovery and early characterizations of CcO, CO has represented an important inhibitory probe for CcO, which mimics O_2.

The results of proton and charge translocation analysis for investigation of the proton pump of various CcO (*1*, *7*–*10*) have been interpreted without assuming that four protons are collected before starting proton pumping as described above. However, these results are essentially consistent with the four proton collection model as described in text S2.

RESULTS

CO movements after pump laser irradiation

CO molecules in the O_2 reduction site without pump laser irradiation (that is, the fully reduced state with CO at Fe_{a3}) (abbreviated as "at dark" hereafter) and 20 ns and 100 μs after pump laser irradiation were located in F_{obs}-F_{calc}. The occupancies of CO of three states were determined by comparing their electron densities with those of two reference waters as described in the "Structure determinations" section in Materials and Methods. The F_{obs}-F_{calc} maps of the O_2 reduction site (Fig. 2A) show CO migration to Cu_B at 20 ns and CO release from Cu_B at 100 μs. The CO movements are also obvious in $F_{(20\ ns\ or\ 100\ \mu s)}$–$F_{(dark)}$ difference electron density maps shown in Fig. 2B and in the IR results (fig. S1). In $F_{(20\ ns)}$–$F_{(dark)}$ difference electron density map, a significant migration of Cu_B toward Fe_{a3} is detectable as a red cage above the Cu_B position in the figure. The CO peak heights of the dark structure and the structures measured 20 ns and 100 μs after CO photolysis are 1.34, 0.99, and 0.22, respectively, relative to the averaged reference peak height of the two water molecules (table S1). The weak peak at 100 μs does not appear in the drawing at a σ level identical to the dark structure and the structure

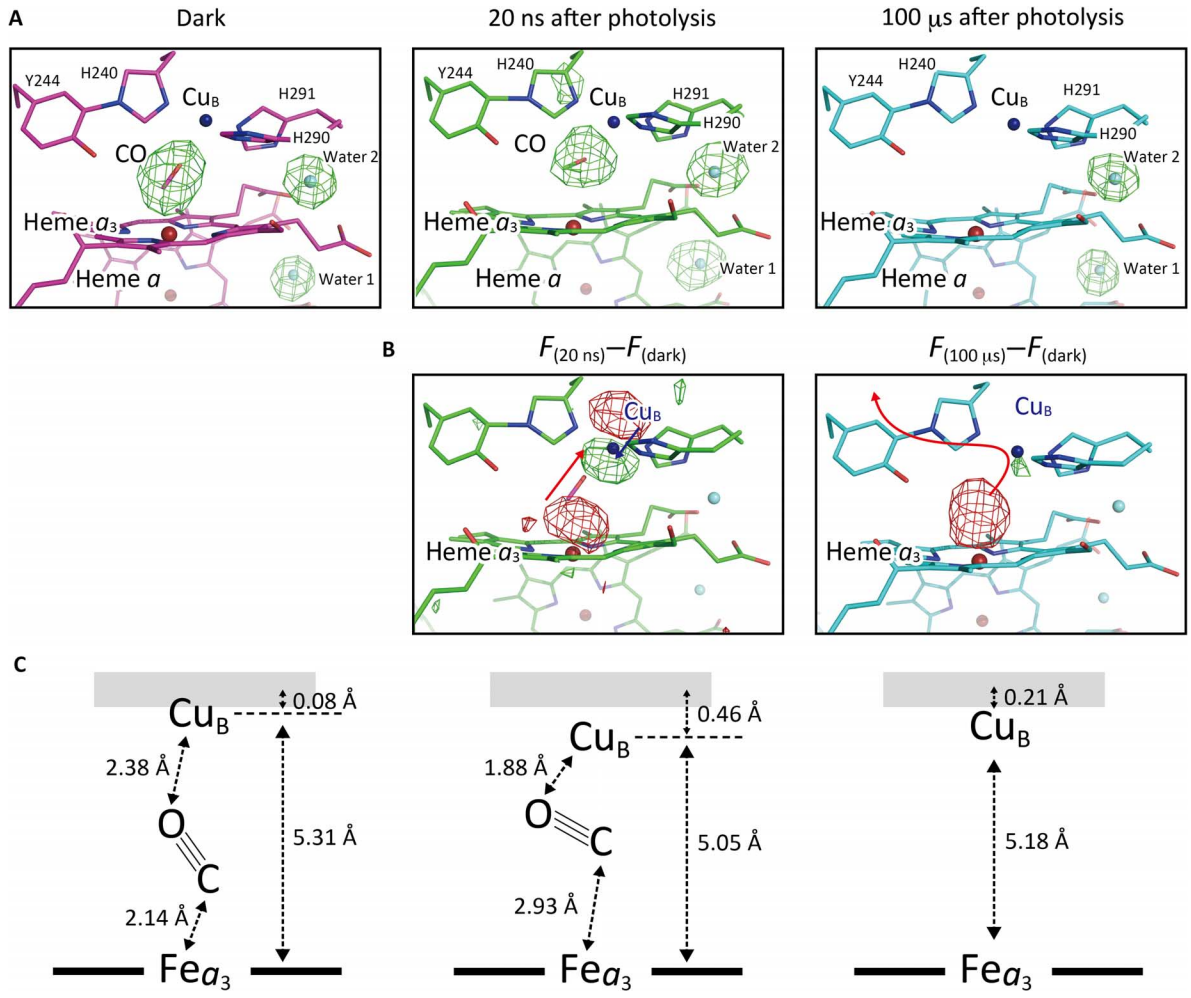

Fig. 2. Structures of the O_2 reduction site of the CO-bound fully reduced state at dark and 20 ns and 100 μs after photolysis. (**A**) F_{obs}-F_{calc} difference electron density maps at 3.5σ and structural models are illustrated. Purple spheres are iron ions, blue spheres are copper ions, and light blue spheres are oxygen atoms of water molecules. Blue and red sticks indicate nitrogen and oxygen atoms, respectively. Red, green, and light blue sticks are the other atoms of the structures measured at dark and 20 ns and 100 μs after photolysis, respectively. CO, Water 1, and Water 2 were not included in the structure refinement. Significant electron density assignable to the CO molecule between Fe_{a3} and Cu_B is not detectable in the 100 μs structure at the σ level in the figure. (**B**) The $F_{(20\ ns\ or\ 100\ \mu s)}$–$F_{(dark)}$ difference electron density maps at the +5.0/−5.0σ level are shown as green/red mesh. The difference density maps show the directions of CO and Cu_B movements and are indicated by red and blue arrows, respectively. (**C**) Geometries of CO in the O_2 reduction site in the structures measured at dark and 20 ns and 100 μs after photolysis. The thick gray line at the top of each structure shows a side view of the Cu_B coordination plane consisting of three imidazole nitrogen atoms.

measured 20 ns after photolysis. The lower electron density measured for the bound CO in the 20-ns structure relative to the electron density of the dark structure corresponds to a higher temperature factor of the CO at Cu_B in the 20-ns structure, as the IR results shown in fig. S1 suggest complete CO saturation at Cu_B at 20 ns (details regarding the time-resolved IR analyses in the single crystalline state are included in text S3 and fig. S1). The electron density peak of 0.22 near Cu_B, seen in the F_{obs}-F_{calc} map measured 100 μs after photolysis, is consistent with the IR results provided in fig. S1, showing the presence of residual (24%) CO bound to Cu_B at 100 μs. The CO ligand geometries are illustrated schematically in Fig. 2C. The Cu_B position is indicated by the Fe_{a3}-Cu_B distance and displacement from the plane consisting of three imidazole nitrogen atoms coordinating to Cu_B (designated as the Cu_B coordination plane). The plane is parallel to the heme a_3 plane. The direction of CO binding (CO or OC) indicated in the figure is tentative. Cu_B is sensitively influenced by the CO binding state, giving the shortest Fe_{a3}-Cu_B distance and the largest displacement from the Cu_B coordination plane 20 ns after photolysis in a tetragonal coordination distorted from the trigonal planar coordination (table S2). The Fe_{a3}-Cu_B distances and the displacements from the Cu_B coordination plane in the structures at dark and 20 ns and 100 μs after photolysis are highly comparable to those of the static x-ray structures of the CO-bound fully reduced CcOs at 280 K [Protein Data Bank (PDB) ID, 3AG1] and at 100 K (PDB ID, 3AG2) and of the ligand-free fully reduced CcO at 50 K (PDB ID, 5B1B), respectively. In CO-bound fully reduced CcOs at 280 and 100 K, CO is bound at Fe_{a3}^{2+} and Cu_B^{1+}, respectively (*1*). A comparison for these x-ray structures shown in table S2 strongly suggests that the present time-resolved x-ray structure determinations for the O_2 reduction site and helix X are successful. Furthermore, consistent with the static x-ray structural results, the present time-resolved x-ray results show that the proton storage site includes a fixed H_2O molecule (HOH10 in Fig. 1B) hydrogen-bonded to H291, one of the Cu_B ligands (*5*).

The time-resolved structural changes in the heme a_3 region after CO photolysis compared with the redox-coupled changes occurring in bacterial CcO

To monitor the time-resolved structural changes in the protein moiety after CO photolysis, the structures of the CO-bound state at dark and 20 ns and 100 μs after photolysis were superimposed on the ligand-free fully reduced state (the open structure; PDB ID, 5B1B) with least-squares fitting of the main-chain atoms of subunit I (consisting of 514 amino acids) using the COOT (Crystallographic Object-Oriented Toolkit) program (*11*), as shown in Fig. 3 (A and B). Upon CO release by photolysis, as illustrated by thin stick models, a segment of helix X, including the residues 380 to 384, which is located close to the vinyl group at the C-pyrrole ring (using the PDB ring naming scheme), undergoes a significant conformational change in its main chain, whereas only small translational shifts with no obvious conformational changes are detectable in helices VIII and IX surrounding heme a_3 (Fig. 3A). Upon complete reduction of the fully oxidized bacterial CcO (*12*), a large translational shift is identified in helix VIII, as well as a conformational transition in helix X. Similar structural changes in helices VIII and IX significantly greater than those of bovine CcO are expected to occur upon CO release from bacterial CcO because CO release induces conformational changes closely similar to those observed upon complete reduction of the fully oxidized

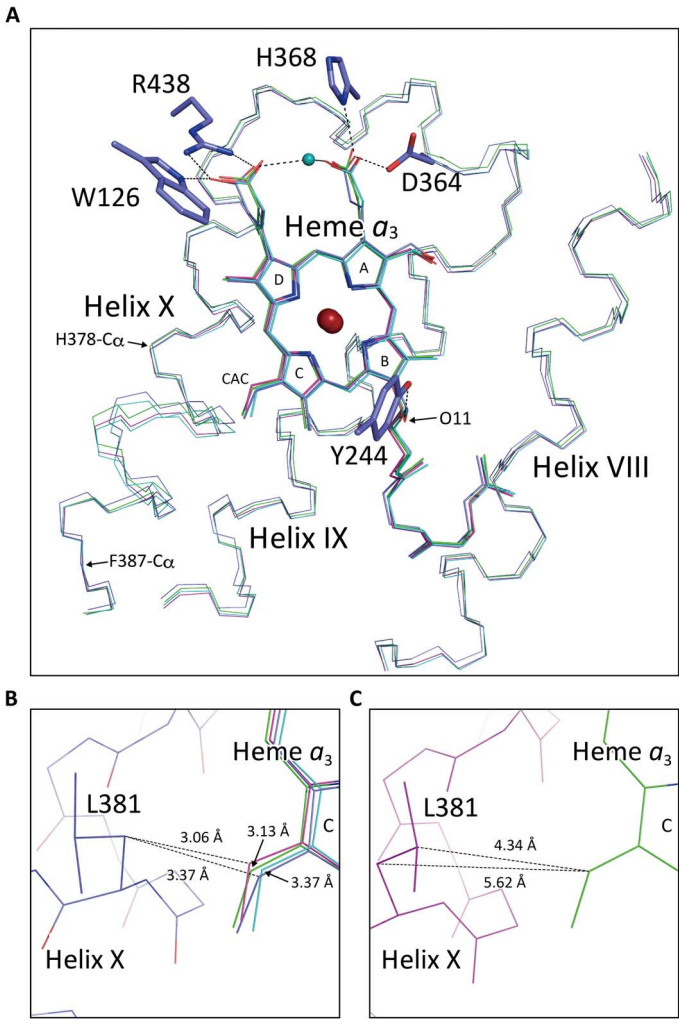

Fig. 3. Structural comparison of the heme a_3 region in the structures measured at dark and 20 ns and 100 μs after photolysis. (**A**) Each structure is superposed on that of the fully reduced ligand-free state (PDB ID, 5B1B) by least-squares fitting of the main-chain atoms of subunit I. The dark structure is pink, the structure measured 20 ns after photolysis is green, the structure measured 100 μs after photolysis is light blue, and the structure in the ligand-free fully reduced state is blue. Dark blue sticks and red spheres of heme a_3 indicate nitrogen atoms and iron ions, respectively. The light blue sphere denotes the location of Water 2 shown in Fig. 2A. Amino acid side chains interacting with the heme a_3 by hydrogen bonds are drawn in thick stick models for the fully reduced state. These interactions are fully preserved in all of the time-resolved structures. Labels, A, B, C, and D in the heme designate the PDB naming of the pyrrole rings. "CAC" indicates one of the carbon atoms of the vinyl group covalently bonded to the C-ring. (**B**) Close-up of the vinyl group regions in (A). The structures of heme a_3 and the Cα drawings of protein regions in the structures at dark and measured 20 ns and 100 μs after photolysis are illustrated using the same color code as in (A). Helix X of the ligand-free fully reduced state (PDB ID, 5B1B) is indicated by a thin stick model, where oxygen atoms are red and the other atoms are blue. The distances between the β carbon of L381 and CAC in the dark structure (pink) and the ligand-free fully reduced state structure (blue) are indicated by the digits with corresponding dotted lines. Those in the 20-ns structure (green) and 100-μs structure (blue) are given by the digits with corresponding arrows. (**C**) Heme a_3 in the structures measured 20 ns after photolysis. Helix X structure measured at dark is indicated by a red stick model.

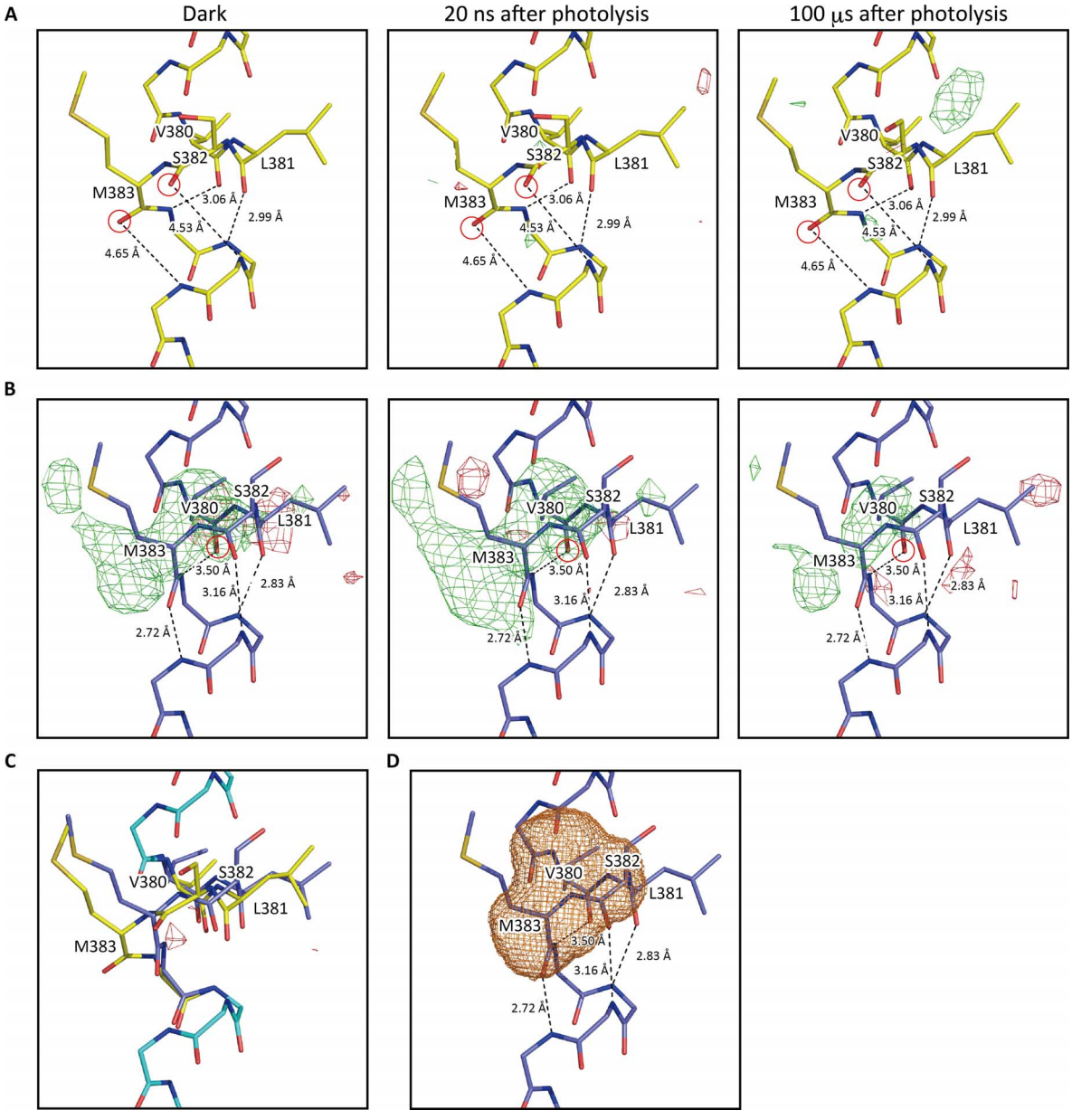

Fig. 4. F_{obs}-F_{calc} difference electron density maps of the structures measured at dark and 20 ns and 100 μs after photolysis. The structure factors of F_{calc} were calculated from the closed and open structures of helix X with two bulges at S382 and M383 (**A**) and with one bulge at V380 (**B**), and the F_{obs}-F_{calc} difference electron density maps were drawn at 3.5σ together with the closed and open structures of helix X, respectively. The red circles mark the location of these bulges. (**C**) The F_{obs}-F_{calc} difference electron density map of the structure measured 100 μs after photolysis, where the structure factors of F_{calc} were calculated with multiple structures of helix X (55% closed structure with the two bulges and 45% open structure with the one bulge), is drawn at 3.5σ together with the open and closed structures of helix X. (**D**) Location of the cavity detectable in the ligand-free fully reduced state. The cavity is indicated with a brown cage together with the ligand-free fully reduced structure of helix X.

bovine CcO. An x-ray structure of CO-bound bacterial CcO has not yet been reported. Among the four pyrrole rings, the greatest movement is detectable in the C-ring, and the least movement is detectable in the A-ring (in PDB naming). This was identified previously in a structural comparison of fully oxidized and fully reduced bacterial CcOs (*12*, *13*).

Five amino acid side chains are hydrogen-bonded to heme a_3 peripheral groups of the ligand-free reduced CcO, as shown in thick stick models, including Y244 covalently linked to one of the three imidazole groups ligated to Cu_B (Fig. 3A). No significant change in these hydrogen bonding structures is induced by CO release. In contrast, a bacterial CcO has a hydrogen bond between the tyrosine and hydroxyfarnesylethyl groups, which is broken to receive a water molecule to bridge the two groups upon complete reduction of the fully oxidized CcO (PDB IDs, 2GMS and 3FYE) (*12*). As described above, complete reduction of the fully oxidized CcO induces structural changes closely resembling those observed upon CO release in bovine CcO. Thus, CO release in the bacterial CcO is likely to induce

conformational changes closely similar to those upon complete reduction. The translational shift in heme a_3 of bovine CcO upon CO release is significantly smaller than the shift upon complete reduction of bacterial CcO. The magnitudes of the translational shifts of one of the carbon atoms of the vinyl group covalently bonded to the C-ring (which is designated CAC in the PDB naming scheme) and the hydroxyfarnesylethyl OH group (O11 in the PDB naming scheme) upon CO binding to bovine CcO are 0.54 and 0.34 Å, respectively, whereas the shifts that occur upon oxidation of the fully reduced bacterial CcO are 1.80 and 2.22 Å, respectively.

Time-resolved structural changes in the heme a_3 vinyl group

Figure 3B is a magnified view of the heme a_3 vinyl group region, which includes the structure of helix X near L381 in the ligand-free fully reduced state as a reference, where oxygen atoms are red and the other atoms are blue. The distances between the β-carbon atom of L381 of helix X in the ligand-free fully reduced state and the CAC in the dark structure, the structure measured at 20 ns and 100 μs, and the ligand-free fully reduced structures are 3.06, 3.13, 3.37, and 3.37 Å, respectively (table S2). Collectively, these results indicate unidirectional movement of the vinyl group along with CO migration and release after photolysis. Movement of the plane of heme a_3 is essentially concerted with CO migration and release. The vinyl groups of the dark structure and the structure measured 20 ns after photolysis (the red and green structures in Fig. 3B) are located too close to L381 in the ligand-free reduced state to be stable. The significant van der Waals interaction changes that occur upon the vinyl group migration are likely to induce conformational changes in L381. A hypothetical structure in which heme a_3 in the structure measured 20 ns after photolysis is superimposed on the static helix X structure near L381 at dark (Fig. 3C) (which was obtained from a structural analysis of helix X, as described in the next paragraph) shows that L381 at dark is located quite far from the vinyl group. The C_β and C_γ atoms of the side chain are 5.62 and 4.34 Å from the vinyl CAC atom, as illustrated in Fig. 3C. Thus, it appears that L381 senses the conformational changes of the vinyl group.

Time-resolved conformational changes in helix X

Both the F_{obs}-F_{calc} maps in the helix X region measured at dark and 20 ns after photolysis, calculated using the structure, which includes two bulges at S382 and M383 that define the closed conformation, indicate no significant residual density (see Fig. 4A). On the other hand, the F_{obs}-F_{calc} maps calculated using the structure with only one bulge at V380 (the open structure) have large positive (green) and negative (red) residual densities, as shown in Fig. 4B. The location of the positive electron density in Fig. 4B in both the dark structure and the structure measured 20 ns after photolysis is essentially identical to that of the water cavity of the water channel of the H-pathway (Fig. 4D). These results indicate that helix X in the dark structure and in the structure measured 20 ns after photolysis adopts the closed structure. The closed and open structures both provide significant residual densities for the F_{obs}-F_{calc} maps in the structure measured 100 μs after photolysis, as shown in Fig. 4, A and B, respectively. The refinement of the structure composed of 55% closed structure and 45% open structure converges to almost the same averaged *B*-factors of helix X and significantly reduced residual electron density (Fig. 4C). Consequently, the occupancies of two structures in the multiple conformations were estimated to be 55% closed and 45% open. Thus, at 100 μs, the closed-to-open structural transition is detectable only for 45% of the structure, although 76% of CO has been released from Cu_B, as indicated by both x-ray and IR data (more detailed descriptions of these x-ray structure determinations are provided in the "Structure determinations" section in Materials and Methods, and the accuracy of the structure determination is described in table S3). Therefore, CO release

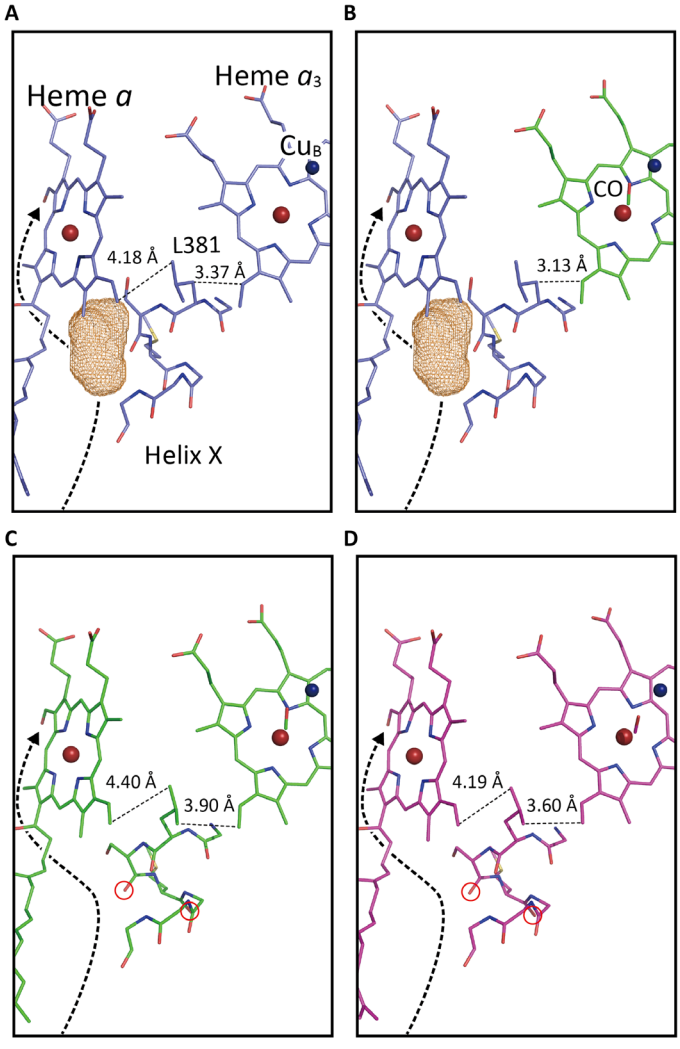

Fig. 5. Proposed water channel closure process upon CO binding to the O_2 reduction site. Hemes *a* and a_3, CO, and residues 380 to 386 of the helix X are drawn as stick models. The purple, green, and pink structures denote the ligand-free (open) and CO-bound states at Cu_B (closed) and at Fe_{a3} (closed), which are detectable in the ligand-free fully reduced state, 20 ns after photolysis, and at dark, respectively. Nitrogen, oxygen, and sulfur atoms are indicated by blue, red, and yellow colors, respectively. Fe_a and Fe_{a3} are indicated as red spheres, and Cu_B is shown as a blue sphere. Side chains of residues 380, 385, and 386 are excluded from the models to preserve clarity. The location of the water channel in each panel is marked by the dotted arrow and the brown cage. (**A**) Structure of the reduced state, where the water channel is open as indicated by the cage. (**B**) Predicted structure constructed by introducing the heme a_3 structure 20 ns after photolysis (in which CO is bound to Cu_B) into the arrangement in the ligand-free fully reduced state. This predicted structure suggests that CO binding to Cu_B induces a significant shift of the vinyl group of heme a_3 toward L381. (**C**) X-ray structure experimentally obtained 20 ns after photolysis, showing significant conformational changes in L381 and bulge formation at S382 and M383, as indicated by red circles. (**D**) Dark structure. After closure of the channel, CO migrates to Fe_{a3} from Cu_B without inducing any conformational change in helix X.

from Cu_B and conversion to the open conformation are not completely concerted.

DISCUSSION

The coexistence of the closed and open conformations at 100 μs indicates that CO release from Cu_B drives the transition of the closed structure to the open structure by elimination of the two bulges at S382 and M383, which are located adjacent to L381. As described above, migration of the heme a_3 vinyl group driven by CO controls the conformation of L381. These results strongly suggest that a relay system that includes Cu_B, the vinyl group of heme a_3, L381, and S382 exists. Thus, during CO binding to the O_2 reduction site (CcO + CO → CcO-CO), CO binding to Cu_B is most likely to induce the formation of the closed structure using the relay system, as follows: When Cu_B receives CO transferred from outside of the CcO molecule (Fig. 5, A and B), the vinyl group of heme a_3 shifts to change the conformation of L381, which in turn induces the formation of the bulge structures of S382 and M383 (Fig. 5C), which then induce the conformational change in S382 to eliminate the water cavity (illustrated by the change of the brown cage from Fig. 5B to Fig. 5C). After closing the channel, CO migrates to Fe_{a3} from Cu_B without inducing any additional conformational change in the helix X (Fig. 5, C and D).

The present time-resolved x-ray structure analyses showed that consistent to the decrease in the Fe_{a3}-Cu_B distance upon CO binding to Cu_B in the structure measured 20 ns after photolysis, CO binds to Cu_B in a tetragonal coordination distorted from the trigonal planar coordination (Fig. 2C and table S2). As described in Fig. 1B, one of the Cu_B ligand, H291, is hydrogen-bonded to a water molecule (HOH10) in the Mg-containing water cluster (*5*). The above experimental results suggest that Cu_B has enough flexibility to sense the proton saturation in the Mg-containing water cluster. Protonation of HOH10 upon proton saturation of the Mg-containing cluster appears to induce some distortion of the essentially equilateral trigonal planar coordination of the three imidazoles to Cu_B^{1+} ion, as shown in Fig. 2, to increase the ligand binding affinity of Cu_B^{1+}. High-resolution analyses

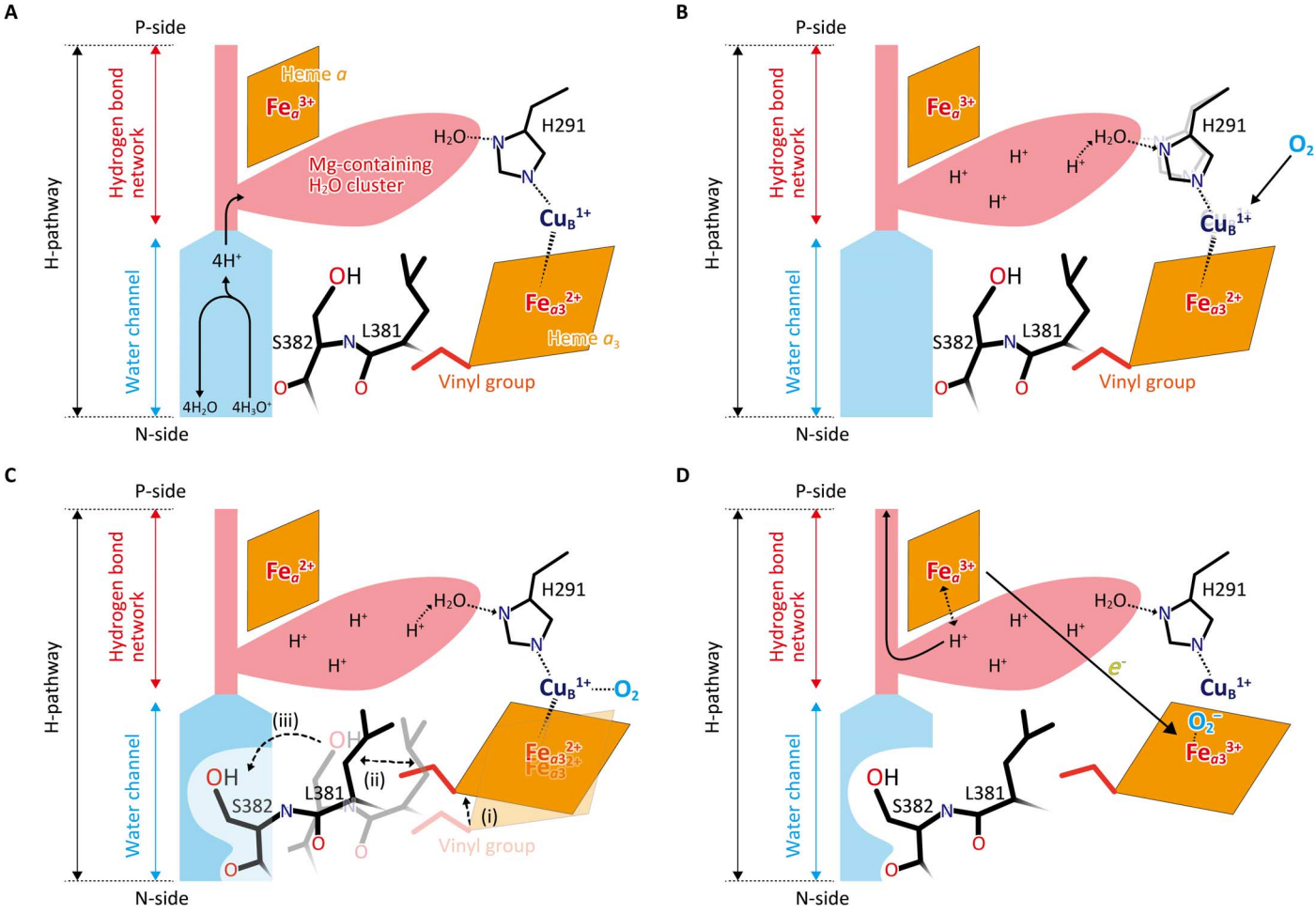

Fig. 6. A schematic representation of a proposal for the water channel closure mechanism. (**A**) The O_2 reduction site composed of Cu_B and Fe_{a3} is in the fully reduced state under turnover conditions. The Mg-containing H_2O cluster is the H^+ storage site, which is connected to Cu_B via H291 and a fixed water molecule (HOH10 in Fig. 1) in the storage site. The heme a_3 vinyl group is in van der Waals contact with L381. Protons are transferred by H_3O^+ through the open water channel. (**B**) Increase in the O_2 affinity of Cu_B^{1+} caused by distortion of the regular trigonal coordination of Cu_B^{1+}, which is induced by protonation of the fixed water upon full protonation of the Mg-containing H_2O cluster. (**C**) Closure of the water channel upon O_2 binding to Cu_B as follows: (i) migration of the plane of heme a_3, (ii) structural change of L381, and (iii) formation of the bulge at S382 to close the channel. (**D**) Proton pump after the channel closure. After migration of O_2 to Fe_{a3}^{2+}, Fe_a^{2+} is oxidized to pump protons.

of pH effects on the Cu_B structure are necessary for obtaining experimental confirmation of the Cu_B function responding to the protonation of HOH10, as proposed here.

These structural features have led us to propose a mechanism for closure of the water channel, which is shown schematically in Fig. 6. In Fig. 6A, the O_2 reduction site is in the fully reduced state, with both of its metals (Cu_B and Fe_{a3}) in the reduced state, under turnover conditions. The channel is opened and heme *a* is likely to be in the oxidized state. Protons are transferred from the N-side (as hydronium ions) to the Mg-containing water cluster. When proton saturation is attained in the cluster, the protonated HOH10 perturbs the coordination structure of Cu_B to increase O_2 affinity (Fig. 6B). Once O_2 is trapped at Cu_B, the water channel closure is induced through the conformational relay system shown in Fig. 5, as follows (Fig. 6C): (i) The plane of heme a_3 migrates; (ii) van der Waals interactions are altered between the vinyl group of heme a_3 and L381; and (iii) a bulge forms at S382 when L381 moves to close the water channel. This process is followed by O_2 transfer to Fe_{a3} (*1*–*3*), giving $Fe_{a3}{}^{3+}$-$O_2{}^{-}$, which readily extracts electrons from heme *a* when it is reduced (Fig. 6D). The heme *a* oxidation induces electrostatic repulsion against protons in the storage site (Fig. 6D). This causes obligatory pumping of protons to the P-side because the water channel is closed.

The present time-resolved analyses show that CO release from Cu_B is not completely concerted with formation of the open structure. Thus, the reverse process (CO binding to Cu_B) is unlikely to be tightly coupled with formation of the closed structure. This is also the case with respect to CO (and thus O_2) binding to Fe_{a3} because the relay system including heme a_3–L381–S382 is critical for coupling between O_2 binding to Fe_{a3} and the S382 structural change as in the case of the coupling between O_2 binding to Cu_B and the S382 structural change. The weak coupling between O_2 binding to Fe_{a3} and S382 structural change is likely to allow heme *a* oxidation to be initiated before closure of the water channel, whereas binding of O_2 to Cu_B does not induce heme *a* oxidation (*1*). Thus, although Cu_B/S382 coupling is not completely tight, closure of the water channel by binding of O_2 to Cu_B, before O_2 binding to Fe_{a3} as in Fig. 6, provides effective blockage against the backflow of protons for pumping.

Note that direct observation of the water channel structural change process by the time-resolved x-ray structure analysis at high resolution, which is enabled only by the present SF-ROX method (*6*) using many large single crystals, shows the overall water channel closure process of CcO starting from Cu_B migration to the bulge formation at S382 as a time-resolved atomic event. The weak coupling between Cu_B and S382 could not be identified by other methods presently available than the time-resolved x-ray structure analysis by XFEL.

MATERIALS AND METHODS

Experimental design

A newly developed SF-ROX method (*6*) using many large single crystals was used in the present project because our previous static x-ray structure analyses (*5*) strongly suggest that time-resolved x-ray structure analyses at high resolution is prerequisite for understanding the water channel closure mechanism of CcO. Furthermore, because protein crystal packing is likely to influence the physiological process in the protein, the time-resolved IR technique is applied for monitoring the CO movements in CcO in the crystals under the conditions of the time-resolved x-ray structure analyses.

In contrast to various photoreactions of excitable chromophores, such as *p*-coumaric acid (in photoactive yellow protein) and retinal (in bacteriorhodopsin), spontaneous reversal of photolysis of heme Fe-CO is essentially absent. Therefore, the quantum yield of the photolysis is close to unity (*14*). Complete photolysis can be attained by increasing the pump-pulse energy. The pump-pulse energy required for complete photolysis was evaluated by visible absorption spectroscopy of heme, which can quantitatively evaluate the photolysis of Fe_{a3}-CO, as described in the Supplementary Materials.

Setup for time-resolved IR spectroscopy on crystals

Time-resolved IR spectroscopy measurement on crystals was performed at 4°C using a system developed based on a femtosecond IR laser (*15*). Briefly, a femtosecond IR pulse was used as the light source, generated by difference frequency generation with an optical parametric amplifier, which was pumped at 1 kHz by the output of a Ti:sapphire oscillator/regenerative amplifier system (Micra-5/Legend-Elite-HE+USP-III/TOPAS-Prime-Plus, Coherent). IR spectra were recorded at 200 Hz using a spectrograph (TRIAX 190, HORIBA Jobin Yvon) coupled to a multichannel MCT (mercury cadmium telluride) detector array and a boxcar integrator system (FPAS-0144-2424, Infrared Systems Development). CO photolysis was induced (from one direction) by the 4-ns, 532-nm output from a Nd:YAG (yttrium aluminum garnet) laser (Minilite-II, Continuum) at 2 Hz, with a low energy of ~20 μJ (<60% photolysis) to avoid photodegradation of the sample. At the sample point, the pump beam diameter was ca. 300 μm, and the probe beam diameter was ca. 130 μm. The pump polarization was adjusted to maximize the excitation efficiency. The pump-probe delay times were controlled by a pulse generator (DG645, Stanford Research Systems) with a timing jitter of ±0.5 ns.

The spectra in the region from 1930 to 2090 cm^{-1} were measured on the {010} face of a $P2_12_12_1$ CcO crystal mounted in the flow cell with a taper-shaped channel. To stabilize the CO-bound form during data accumulation, the CO-saturated mother liquor [40 mM sodium phosphate buffer (pH 5.7), containing 0.2% (w/v) *n*-decyl-β-D-maltoside, 40% (v/v) ethylene glycol, and 8% (w/v) polyethylene glycol 4000, supplemented with 7.5 mM sodium dithionite, 5 mM glucose, 1 μM glucose oxidase, and 0.5 μM catalase] was continuously flowed. The experimental results are given in fig. S1. The machine accuracy was 6 cm^{-1} for the determination of the peak frequencies.

Setup for time-resolved visible absorption spectroscopy on crystals

CO photolysis was induced (from one direction) by the 4-ns, 532-nm pump pulse from a Nd:YAG laser (Minilite-II, Continuum) at 2 Hz, whereas time-resolved spectra were measured at 20 Hz using a fiber-coupled spectrometer (USB2000+, Ocean Optics) with a microsecond white-light pulse from a Xe flash lamp (L7684, Hamamatsu Photonics). The delay times were adjusted by a pulse generator (DG645, Stanford Research Systems) with a timing jitter of 40 ns. The pump beam diameter focused on the crystal was ca. 220 μm, and the probe beam diameter focused on the crystal was ca. 100 μm. The pump polarization was adjusted to minimize the excitation efficiency to gain insight into the excitation efficiency under the challenging pump conditions.

The excitation efficiency was estimated by $|\Delta A_{620} - \Delta A_{590}|$ in the time-resolved difference spectrum, compared with the value measured from the static difference spectrum of the fully reduced form minus the CO-bound form. The static spectra were measured during the

preparation of the CO-bound CcO crystal, as follows: The resting oxidized CcO crystal was first mounted in the flow cell with solution 1 [40 mM sodium phosphate buffer (pH 5.7), containing 0.2% (w/v) *n*-decyl-β-D-maltoside, 40% (v/v) ethylene glycol, and 8% (w/v) polyethylene glycol 4000]. [The resting oxidized CcO was prepared from bovine heart muscle and crystallized as described previously (*16*).] Then, solution 1 supplemented with 8.0 mM sodium dithionite, 5 mM glucose, 1 μM glucose oxidase, and 0.5 μM catalase (solution 2) was flowed to generate the fully reduced form. After measurement of the static spectrum of the fully reduced form, the CO-saturated solution 2 (solution 3) was flowed to generate the CO-bound form, and its static spectrum was measured. The CO-bound CcO crystal was kept under continuous flow of solution 3 during the time-resolved measurement. Time-resolved visible absorption difference spectra of the heme in CcO 50 μs after CO photolysis in the crystalline phase at 4°C with various pump energies obtained under the above conditions are shown in fig. S2.

Setup for time-resolved x-ray crystallography

The 4-ns, 532-nm output from a Nd:YAG laser (Minilite-I, Continuum) was used as the pump pulse for CO photolysis. The laser (10 Hz) was synchronized with XFEL (10 Hz) through a pulse generator (DG645, Stanford Research Systems) with a timing jitter of ±0.5 ns. An optical beam shutter (SH05, Thorlabs) was placed in the pump beam path and synchronized with the x-ray beam shutter, both of which were opened by a trigger from the beamline control software BSS (Beamline Scheduling Software) (*17*) when a diffraction image was collected ("pump-on" data). During diffraction data collection on the CO-bound form ("pump-off" data), the optical shutter was kept closed.

To induce CO photolysis with a high yield close to unity in a large crystal, the pump beam was divided into two beams using a 50:50 beam splitter and focused onto the crystal from two directions (from the front and back sides of the crystal) nearly along the x-ray axis (only 2° off). This pump geometry provided a high pump-photon density at the pump–x-ray interaction volume in the crystal and was found to enhance the excitation efficiency. A novel portable optical system, coupled to a diffractometer, was used for the pump illumination. The details of the optical system have been reported (*18*).

The same optical system was also used for on-line visible absorption spectroscopy by introducing a visible white light (from one direction) on-axis with the pump beam using a dichroic mirror. Static visible absorption spectra were measured for all the crystals mounted to the diffractometer, and only the diffraction data on the crystals exhibiting the spectrum of CO-bound form, both before and after the diffraction data collection, were used for structural analysis. The pump and white light beams were focused on the crystal with ca. 200 and 100 μm diameter, respectively. The pump energy was 200 μJ (100 μJ from each direction) at the crystal, which produces 100% CO photolysis efficiency.

The diffraction images were collected with and without pump laser irradiation at 4°C. The diffractometer with some modifications from its previously reported version was set up in EH4c/BL3 at SACLA (SPring-8 Angstrom Compact free electron LAser) (*18*). As the modifications to accommodate the pump-probe experiment at 4°C, the optical system described above was placed in the space surrounding the crystal sample, and the cryostat was replaced with a crystal humidity controller for the HAG (humid air and glue-coating) method described below. The x-ray pulse parameters for the dark or the 100 μs and for the 20 ns were as follows: photon count at the sample position: 8.9×10^{10} photons, 9.3×10^{10} photons; pulse frequency: 10 Hz, 10 Hz; photon energy: 10.0013 keV, 9.9967 keV; photon energy bandwidth: 0.4% [full width at half maximum (FWHM)] (43 eV), 0.4% (FWHM) (40 eV); beam size at the sample position: 4.8 (H) × 4.0 (V) μm^2, 4.2 (H) × 3.0 (V) μm^2; shot-to-shot variation in photon energy: 0.1% (SD) (10 eV), 0.1% (SD) (10 eV); and shot-to-shot variation in intensity at BM1: 14% (SD) (75 μJ/530 μJ), 13% (SD) (71 μJ/550 μJ). The data collection procedure was the same as described for the previous XFEL experiment for damage-free crystallography (*6*). The distance between each irradiation point was set to 50 μm in the horizontal direction for any rotation angle. The vertical step size was varied depending on the rotation angle to maintain a 50-μm distance between two neighboring beam footprints. The delay times between irradiation of the pump laser and the XFEL pulses were 20 ns and 100 μs. Each set of pump-probe measurements was conducted at <1 Hz so that photoproducts were not accumulated during each measurement. During the diffraction data collection, the crystal was maintained at 4.5° to 5°C and 98% relative humidity by using the HAG method (*19*). The crystal was coated with 5% (w/v) polyvinyl alcohol aqueous solution (an average polymerization degree of 8000) containing 2% (w/v) ethylene glycol and 1% (w/v) polyethylene glycol 4000. The diffraction data obtained without the pump laser irradiation and at 20 ns and 100 μs after the pump laser irradiation were collected from 40, 24, and 43 crystals (0.5 mm in the largest dimension), respectively.

XFEL data processing

Charge-coupled device (CCD) detector images without diffraction patterns were identified using the DISTL program (*20*) and removed before data processing. Bragg peak intensity integration, postrefinement, and merging were performed using the cctbx.xfel program suite (*21*) and the prime program (*22*), which are both included in the CCTBX library (*23*). We modified some lines of code to suit our purposes as described below (the modified version is available at https://github.com/keitaroyam/cctbx_fork/tree/for_sacla_sfrox). Before integration, image files were converted to pickle format using the modified version of cxi.image2pickle, which marks the pixels belonging to instrumental shadows for exclusion from integration. The mask of the shadows was defined using XDS (*24*) with a manually specified area and XDS functionality to detect beamstop shadows. The beam center coordinates were prerefined by performing a grid search (dark and 100 μs) or by using CrystFEL (*25*) (20 ns). For the dark and the 100 μs data, the beam center coordinates and camera distance were optimized using the first crystal by grid search by minimizing averaged root mean square deviations between predicted and observed spot positions using the cxi.index program. For the 20-ns data, beam center coordinates were optimized using CrystFEL suite version 0.6.1. Randomly selected 100 images were given to indexamajig with the indexing program of MOSFLM (*26*). Geometric parameters including beam center coordinates were refined by geoptimiser by minimizing the discrepancies between predicted spot positions and observed ones. Peak search, indexing, and integration were performed using cxi.index with maximum likelihood refinement of mosaicity and mosaic block size (*27*). By-pattern resolution cutoff was determined with criteria of $I/\sigma(I) > 2.0$, 2.0, and 1.5 for the dark, the 100-μs, and the 20-ns data, respectively (the program was modified to accept user-defined resolution limit criteria). The known unit cell dimensions and crystal symmetry were given to the program. All successfully integrated intensities were given to prime.postrefine, which

performed postrefinement and merged intensities by applying calculated partialities. Polarization correction in prime was modified to match our geometric setup. Because the prime program scales intensities in each pattern by applying the estimated Wilson *B*-factor so that all patterns have zero Wilson *B* values during postrefinement when no external reference data were given, the merged intensities were scaled using the averaged Wilson *B* value. *B*-corrected merged intensities after the second (20 ns) or third (dark and 100 μs) macrocycle were used in downstream structural analyses.

Structure determinations

Structure determinations of the three states were initiated by the molecular replacement (MR) method (*28*). Initial phase angles of structure factors up to 5.0 Å resolution for each state were obtained by using the fully oxidized structure previously determined at 1.5 Å resolution (PDB ID, 5B1A). The phases were extended to each highest resolution by the density modification (DM) method (*29*) coupled with noncrystallographic symmetry averaging (*30*, *31*) using the CCP4 program DM (*32*). The resultant phase angles ($\alpha_{MR/DM}$) were used to calculate the electron-density map (MR/DM map) with Fourier coefficients $|F_{obs}| \exp(i\alpha_{MR/DM})$, where $|F_{obs}|$ is the observed structure amplitude. Inspecting the electron density maps around Asp^{51} of subunit I and the hydroxyfarnesylethyl group of heme *a*, where the oxidized and the reduced CcOs have different conformations, it was confirmed that the phase extension procedure removed the model bias from the map. The structural models built in the MR/DM maps were refined using the REFMAC program. Bulk solvent correction and anisotropic scaling of the observed and calculated structural amplitudes and Translation/Libration/Screw (TLS) parameters were incorporated into the refinement calculation. Because two monomers in the asymmetric unit show different bulk motion (*33*), each monomer was defined as a separate TLS group in the refinement calculation. The individual anisotropic temperature factors for the iron, copper, and zinc atoms were imposed on the calculated structure factors. In the refinement, CO bond length was constrained without restraint being imposed on the distances between CO and two metals of Fe_{a3} and Cu_B. Statistics of the structure refinements are listed in table S3.

Two water molecules (Water 1 and Water 2 in Fig. 2A) near the O_2 reduction site that are highly stable in any bovine CcO crystal have been successfully used as internal standards for quantifying the electron densities of the metal ligands in the O_2 reduction site (*5*). These two water molecules were excluded from the initial stage of refinement calculation to estimate the reliability of electron density of the F_{obs}-F_{calc} map. Figure 2A shows F_{obs}-F_{calc} electron density maps drawn at the 3.0σ level for the structures measured at dark and the 20-ns and 100-μs structures after CO photolysis. Peak heights of the F_{obs}-F_{calc} electron density maps are listed in table S1. The electron density close to heme a_3 is assigned as CO bonding to Fe_{a3} with a C-Fe distance of 1.88 Å, and the distance between Fe_{a3} and Cu_B is 5.32 Å in the structure measured at dark. The structure of the O_2 reduction site is essentially identical to that of CO-bound reduced CcO at 280 K (PDB ID, 3AG1), of which C-Fe_{a3} and Fe_{a3}-Cu_B distances are 1.85 and 5.37 Å, respectively. The electron density map of the 20-ns structure indicates that CO is coordinated to Cu_B in a side-on fashion, and Fe_{a3}-Cu_B distance is 5.00 Å. The lower electron density of the bound CO in the 20-ns structure compared with that of the structure measured at dark corresponds to a higher temperature factor of the bound CO in the 20-ns structure relative to that of the structure determined at dark because the IR results given in fig. S1 strongly suggest complete CO saturation at Cu_B at 20 ns. The electron density between Fe_{a3} and Cu_B decreases to 1.5σ in the 100-μs crystal. The peak height is 99% of the averaged peak height of the reference water molecules in the 20-ns crystal, whereas that in the 100-μs crystal is 22% of the averaged peak height of the reference water molecules. The observation of electron density of the 100-μs structure with 23% CO occupancy of that in the 20-ns structure is consistent with the IR results shown in fig. S1, suggesting 24% occupancy of CO in the 100-μs structure after photolysis. Structure refinement with 30% occupancy of CO close to the Cu_B site converged to an averaged *B*-factor of CO to 40 $Å^2$, which is 1.5-fold higher than that of Cu_B, as is that of the 20-ns crystal. The CO presence of 24% estimated from the IR data is consistent with the x-ray analysis of the 100-μs crystal.

Structures of the helix X (residues 371 to 400 of subunit I) of the dark and 20-ns structures were converged to that of the fully oxidized CcO, whereas that of the 100-μs structure had multiple conformations consisting of the closed and open structures. The residues S382 and M383 of the dark and 20-ns structure are in an α-bulge structural feature, which is also visible in the resting oxidized CcO and the CO-bound reduced CcO at 280 K. V380 of the ligand-free fully reduced CcO is in the α-bulge structure. F_{obs}-F_{calc} difference electron density maps for the 100-μs crystal calculated with the helix X structures of S382, M383-bulge type (closed) or V380-bulge type (open), have significant electron densities corresponding to the helix X structures of the open or the closed type, respectively (Fig. 4). Imposing mixed structures on the residues from 380 to 384 of helix X with different ratios of the open and closed conformations, we conducted structure refinements under constraining of the structures of residues 380 to 384. The averaged *B*-factors of these residues are listed in table S4 for the different ratios of the open and closed structures.

SUPPLEMENTARY MATERIALS

Supplementary material for this article is available at http://advances.sciencemag.org/cgi/content/full/3/7/e1603042/DC1

text S1. A proton pumping mechanism proposed for bacterial CcOs.
text S2. Comparisons of the proton pump mechanism of CcO proposed by x-ray structure analyses with the proton pump mechanism proposed on the basis of charge and proton translocation analyses.
text S3. Time-resolved IR analyses in the single crystalline state.
fig. S1. CO ligand dynamics initiated upon CO photolysis of CcO in the crystalline phase at 4°C.
fig. S2. Time-resolved visible absorption difference spectra of the heme in CcO 50 μs after CO photolysis in the crystalline phase at 4°C with various pump energies.
table S1. The peak height of CO molecule at O_2 reduction site.
table S2. Structural comparison for heme a_3 and Cu_B.
table S3. Statistics of intensity data collection and structure refinement.
table S4. Averaged *B*-factors of the residues from V380 to G384.
References (*35*–*45*)

REFERENCES AND NOTES

1. S. Yoshikawa, A. Shimada, Reaction mechanism of cytochrome *c* oxidase. *Chem. Rev.* **115**, 1936–1989 (2015).
2. S. Yoshikawa, K. Muramoto, K. Shinzawa-Itoh, Proton-pumping mechanism of cytochrome *c* oxidase. *Annu. Rev. Biophys.* **40**, 205–223 (2011).
3. P. R. Rich, A. Maréchal, Functions of the hydrophilic channels in protonmotive cytochrome *c* oxidase. *J. R. Soc. Interface* **10**, 20130183 (2013).
4. K. Muramoto, K. Ohta, K. Shinzawa-Itoh, K. Kanda, M. Taniguchi, H. Nabekura, E. Yamashita, T. Tsukihara, S. Yoshikawa, Bovine cytochrome *c* oxidase structures enable O_2 reduction with minimization of reactive oxygens and provide a proton-pumping gate. *Proc. Natl. Acad. Sci. U.S.A.* **107**, 7740–7745 (2010).
5. N. Yano, K. Muramoto, A. Shimada, S. Takemura, J. Baba, H. Fujisawa, M. Mochizuki, K. Shinzawa-Itoh, E. Yamashita, T. Tsukihara, S. Yoshikawa, The Mg^{2+}-containing water cluster

of mammalian cytochrome *c* oxidase collects four pumping proton equivalents in each catalytic cycle. *J. Biol. Chem.* **291**, 23882–23894 (2016).
6. K. Hirata, K. Shinzawa-Itoh, N. Yano, S. Takemura, K. Kato, M. Hatanaka, K. Muramoto, T. Kawahara, T. Tsukihara, E. Yamashita, K. Tono, G. Ueno, T. Hikima, H. Murakami, Y. Inubushi, M. Yabashi, T. Ishikawa, M. Yamamoto, T. Ogura, H. Sugimoto, J.-R. Shen, S. Yoshikawa, H. Ago, Determination of damage-free crystal structure of an X-ray–sensitive protein using an XFEL. *Nat. Methods* **11**, 734–736 (2014).
7. S. A. Siletsky, A. A. Konstantinov, Cytochrome *c* oxidase: Charge translocation coupled to single-electron partial steps of the catalytic cycle. *Biochim. Biophys. Acta* **1817**, 476–488 (2012).
8. M. I. Verkhovsky, A. Jasaitis, M. L. Verkhovskaya, J. E. Morgan, M. Wikström, Proton translocation by cytochrome *c* oxidase. *Nature* **400**, 480–483 (1999).
9. D. Bloch, I. Belevich, A. Jasaitis, C. Ribacka, A. Puustinen, M. I. Verkhovsky, M. Wikström, The catalytic cycle of cytochrome *c* oxidase is not the sum of its two halves. *Proc. Natl. Acad. Sci. U.S.A.* **101**, 529–533 (2004).
10. K. Faxén, G. Gilderson, P. Ädelroth, P. Brzezinski, A mechanistic principle for proton pumping by cytochrome *c* oxidase. *Nature* **437**, 286–289 (2005).
11. P. Emsley, B. Lohkamp, W. G. Scott, K. Cowtan, Features and development of *Coot*. *Acta Crystallogr. D Biol. Crystallogr.* **66** (Pt. 4), 486–501 (2010).
12. L. Qin, J. Liu, D. A. Mills, D. A. Proshlyakov, C. Hiser, S. Ferguson-Miller, Redox-dependent conformational changes in cytochrome *c* oxidase suggest a gating mechanism for proton uptake. *Biochemistry* **48**, 5121–5130 (2009).
13. J. Liu, L. Qin, S. Ferguson-Miller, Crystallographic and online spectral evidence for role of conformational change and conserved water in cytochrome oxidase proton pump. *Proc. Natl. Acad. Sci. U.S.A.* **108**, 1284–1289 (2011).
14. F. Schotte, H. S. Cho, V. R. I. Kaila, H. Kamikubo, N. Dashdorj, E. R. Henry, T. J. Graber, R. Henning, M. Wulff, G. Hummer, M. Kataoka, P. A. Anfinrud, Watching a signaling protein function in real time via 100-ps time-resolved Laue crystallography. *Proc. Natl. Acad. Sci. U.S.A.* **109**, 19256–19261 (2012).
15. M. Kubo, S. Nakashima, S. Yamaguchi, T. Ogura, M. Mochizuki, J. Kang, M. Tateno, K. Shinzawa-Itoh, K. Kato, S. Yoshikawa, Effective pumping proton collection facilitated by a copper site (Cu_B) of bovine heart cytochrome *c* oxidase, revealed by a newly developed time-resolved infrared system. *J. Biol. Chem.* **288**, 30259–30269 (2013).
16. M. Mochizuki, H. Aoyama, K. Shinzawa-Itoh, T. Usui, T. Tsukihara, S. Yoshikawa, Quantitative reevaluation of the redox active sites of crystalline bovine heart cytochrome *c* oxidase. *J. Biol. Chem.* **274**, 33403–33411 (1999).
17. G. Ueno, H. Kanda, T. Kumasaka, M. Yamamoto, Beamline Scheduling Software: Administration software for automatic operation of the RIKEN structural genomics beamlines at SPring-8. *J. Synchrotron Radiat.* **12**, 380–384 (2005).
18. M. Sakaguchi, T. Kimura, T. Nishida, T. Tosha, H. Sugimoto, Y. Yamaguchi, S. Yanagisawa, G. Ueno, H. Murakami, H. Ago, M. Yamamoto, T. Ogura, Y. Shiro, M. Kubo, A nearly on-axis spectroscopic system for simultaneously measuring UV-visible absorption and X-ray diffraction in the SPring-8 structural genomics beamline. *J. Synchrotron Radiat.* **23**, 334–338 (2016).
19. S. Baba, T. Hoshino, L. Ito, T. Kumasaka, Humidity control and hydrophilic glue coating applied to mounted protein crystals improves X-ray diffraction experiments. *Acta Crystallogr. D Biol. Crystallogr.* **69**, 1839–1849 (2013).
20. Z. Zhang, N. K. Sauter, H. van den Bedem, G. Snell, A. M. Deacon, Automated diffraction image analysis and spot searching for high-throughput crystal screening. *J. Appl. Crystallogr.* **39**, 112–119 (2006).
21. J. Hattne, N. Echols, R. Tran, J. Kern, R. J. Gildea, A. S. Brewster, R. Alonso-Mori, C. Glöckner, J. Hellmich, H. Laksmono, R. G. Sierra, B. Lassalle-Kaiser, A. Lampe, G. Han, S. Gul, D. DiFiore, D. Milathianaki, A. R. Fry, A. Miahnahri, W. E. White, D. W. Schafer, M. M. Seibert, J. E. Koglin, D. Sokaras, T.-C. Weng, J. Sellberg, M. J. Latimer, P. Glatzel, P. H. Zwart, R. W. Grosse-Kunstleve, M. J. Bogan, M. Messerschmidt, G. J. Williams, S. Boutet, J. Messinger, A. Zouni, J. Yano, U. Bergmann, V. K. Yachandra, P. D. Adams, N. K. Sauter, Accurate macromolecular structures using minimal measurements from X-ray free-electron lasers. *Nat. Methods* **11**, 545–548 (2014).
22. M. Uervirojnangkoorn, O. B. Zeldin, A. Y. Lyubimov, J. Hattne, A. S. Brewster, N. K. Sauter, A. T. Brunger, W. I. Weis, Enabling X-ray free electron laser crystallography for challenging biological systems from a limited number of crystals. *eLife* **4**, e05421 (2015).
23. R. W. Grosse-Kunstleve, N. K. Sauter, N. W. Moriarty, P. D. Adams, The *Computational Crystallography Toolbox*: Crystallographic algorithms in a reusable software framework. *J. Appl. Crystallogr.* **35**, 126–136 (2002).
24. W. Kabsch, XDS. *Acta Crystallogr. D Biol. Crystallogr.* **66**, 125–132 (2010).
25. T. A. White, R. A. Kirian, A. V. Martin, A. Aquila, K. Nass, A. Barty, H. N. Chapman, *CrystFEL*: A software suite for snapshot serial crystallography. *J. Appl. Crystallogr.* **45**, 335–341 (2012).
26. A. G. W. Leslie, H. R. Powell, in *Evolving Methods for Macromolecular Crystallography*, R. J. Read, J. L. Sussman, Eds. (Springer, 2007), vol. 245, pp. 41–51.
27. N. K. Sauter, J. Hattne, A. S. Brewster, N. Echols, P. H. Zwart, P. D. Adams, Improved crystal orientation and physical properties from single-shot XFEL stills. *Acta Crystallogr. D Biol. Crystallogr.* **70**, 3299–3309 (2014).
28. M. G. Rossmann, D. M. Blow, The detection of sub-units within the crystallographic asymmetric unit. *Acta Crystallogr.* **15**, 24–31 (1962).
29. B. C. Wang, Resolution of phase ambiguity in macromolecular crystallography. *Methods Enzymol.* **115**, 90–112 (1985).
30. G. Bricogne, Geometric sources of redundancy in intensity data and their use for phase determination. *Acta Crystallogr. Sect. A* **30**, 395–405 (1974).
31. G. Bricogne, Methods and programs for direct-space exploitation of geometric redundancies. *Acta Crystallogr. Sect. A* **32**, 832–847 (1976).
32. K. Cowtan, DM: An automated procedure for phase improvement by density modification. *Jt. CCP4 ESF-EACBM Newsl. Protein Crystallogr.* **31**, 34–38 (1994).
33. T. Tomizaki, E. Yamashita, H. Yamaguchi, H. Aoyama, T. Tsukihara, K. Shinzawa-Itoh, R. Nakashima, R. Yaono, S. Yoshikawa, Structure analysis of bovine heart cytochrome *c* oxidase at 2.8 A resolution. *Acta Crystallogr. D. Biol. Crystallogr.* **55** (Pt. 1), 31–45 (1999).
34. G. J. Kleywegt, T. A. Jones, Detection, delineation, measurement and display of cavities in macromolecular structures. *Acta Crystallogr. D Biol. Crystallogr.* **50**, 178–185 (1994).
35. K. Shimokata, Y. Katayama, H. Murayama, M. Suematsu, T. Tsukihara, K. Muramoto, H. Aoyama, S. Yoshikawa, H. Shimada, The proton pumping pathway of bovine heart cytochrome *c* oxidase. *Proc. Natl. Acad. Sci. U.S.A.* **104**, 4200–4205 (2007).
36. K. Kamiya, M. Boero, M. Tateno, K. Shiraishi, A. Oshiyama, Possible mechanism of proton transfer through peptide groups in the H-pathway of the bovine cytochrome *c* oxidase. *J. Am. Chem. Soc.* **129**, 9663–9673 (2007).
37. A. A. Konstantinov, S. Siletsky, D. Mitchell, A. Kaulen, R. B. Gennis, The roles of the two proton input channels in cytochrome *c* oxidase from *Rhodobacter sphaeroides* probed by the effects of site-directed mutations on time-resolved electrogenic intraprotein proton transfer. *Proc. Natl. Acad. Sci. U.S.A.* **94**, 9085–9090 (1997).
38. T. Hayashi, Y. Asano, Y. Shintani, H. Aoyama, H. Kioka, O. Tsukamoto, M. Hikita, K. Shinzawa-Itoh, K. Takafuji, S. Higo, H. Kato, S. Yamazaki, K. Matsuoka, A. Nakano, H. Asanuma, M. Asakura, T. Minamino, Y.-i. Goto, T. Ogura, M. Kitakaze, I. Komuro, Y. Sakata, T. Tsukihara, S. Yoshikawa, S. Takashima, *Higd1a* is a positive regulator of cytochrome *c* oxidase. *Proc. Natl. Acad. Sci. U.S.A.* **112**, 1553–1558 (2015).
39. D. Zaslavsky, R. C. Sadoski, S. Rajagukguk, L. Geren, F. Millett, B. Durham, R. B. Gennis, Direct measurement of proton release by cytochrome *c* oxidase in solution during the F→O transition. *Proc. Natl. Acad. Sci. U.S.A.* **101**, 10544–10547 (2004).
40. S. Yoshikawa, K. Shinzawa-Itoh, R. Nakashima, R. Yaono, E. Yamashita, N. Inoue, M. Yao, M. J. Fei, C. P. Libeu, T. Mizushima, H. Yamaguchi, T. Tomizaki, T. Tsukihara, Redox-coupled crystal structural changes in bovine heart cytochrome *c* oxidase. *Science* **280**, 1723–1729 (1998).
41. S. I. Chan, Proton pumping in cytochrome *c* oxidase: The coupling between proton and electron gating. *Proc. Natl. Acad. Sci. U.S.A.* **107**, 8505–8506 (2010).
42. R. Mitchell, P. R. Rich, Proton uptake by cytochrome *c* oxidase on reduction and on ligand binding. *Biochim. Biophys. Acta* **1186**, 19–26 (1994).
43. O. Einarsdóttir, R. B. Dyer, D. D. Lemon, P. M. Killough, S. M. Hubig, S. J. Atherton, J. J. López-Garriga, G. Palmer, W. H. Woodruff, Photodissociation and recombination of carbonmonoxy cytochrome oxidase: Dynamics from picoseconds to kiloseconds. *Biochemistry* **32**, 12013–12024 (1993).
44. J. O. Alben, P. P. Moh, F. G. Fiamingo, R. A. Altschuld, Cytochrome oxidase (a_3) heme and copper observed by low-temperature Fourier transform infrared spectroscopy of the CO complex. *Proc. Natl. Acad. Sci. U.S.A.* **78**, 234–237 (1981).
45. R. B. Dyer, K. A. Peterson, P. O. Stoutland, W. H. Woodruff, Picosecond infrared study of the photodynamics of carbonmonoxy-cytochrome *c* oxidase. *Biochemistry* **33**, 500–507 (1994).

Acknowledgments

Funding: This work was supported by the X-ray Free Electron Laser Priority Strategy Program of the Japanese Ministry of Education, Culture, Sports, Science and Technology (MEXT) (T.O. and H.A.). T. Kimura is supported by the K-CONNEX program. This work was supported by Japan Science and Technology Agency (JST) Core Research for Evolutional Science and Technology (K.H., G.U., and T.T.), JST Precursory Research for Embryonic Science and Technology (M.K. and K.H.), and Pioneering Project "Dynamic Structural Biology" of RIKEN (M.K. and M. Yamamoto) and by Photon and Quantum Basic Research Coordinated Development Program (to T.T., S. Yoshikawa, and K.S.-I.), provided by MEXT. Support is also provided by Japan Society for the Promotion of Science KAKENHI grants 26291033 (to S. Yoshikawa), 15K18493 (to A.S.), and 15H03841 (to M.K.) and Innovative Areas "3D Active-Site Science" 15H01055 (to M.K.) and by Machine Tool Engineering Foundation (R.K. and J.Y.). **Author contributions:** All authors contributed to the diffraction experiments at SACLA and discussed and commented on the results and the manuscript. A.S., M.K., and S.B. planned experiments. S.O., K.T., and M. Yabashi contributed to beamline operation. G.U., H.M., T. Kumasaka, T. Kimura, M.S., R.K., J.Y., and T.O. contributed to the development of the experimental instruments. K.S.-I., J.B., K.H., Y.E., A.M., K.Y., K.H., M. Yamamoto, T.N., Y.Y., S. Yanagisawa, and E.Y. conducted protein purification, crystallization, diffraction, and IR experiments and data analyses. S. Yoshikawa, A.S.,

T.T., and H.A. wrote the manuscript. **Competing interests:** T.O., M.S., and S. Yanagisawa are visiting scientists at RIKEN. The authors declare that they have no competing interests. **Data and materials availability:** All data needed to evaluate the conclusions in the paper are present in the paper and/or the Supplementary Materials. Additional data related to this paper may be requested from the authors. The atomic coordinates and structure factors (IDs 5X1F, 5X1B, and 5X19) have been deposited in the PDB (www.pdbj.org/). The best condition for the diffraction data collection at 4°C using the HAG method was determined in the SPring-8 at BL38B1 under proposals 2014A1293, 2014B1483, 2015A1115, 2015B2115, and 2016B2732. Diffraction data were collected in the SACLA facility at BL3 under proposals 2014A8036, 2014B8055, 2015A8030, 2015A8053, 2015B8032, 2015B8051, 2016A8034, 2016A8050, 2016B8053, and 2016B8070.

Submitted 2 December 2016
Accepted 14 June 2017
Published 14 July 2017
10.1126/sciadv.1603042

Citation: A. Shimada, M. Kubo, S. Baba, K. Yamashita, K. Hirata, G. Ueno, T. Nomura, T. Kimura, K. Shinzawa-Itoh, J. Baba, K. Hatano, Y. Eto, A. Miyamoto, H. Murakami, T. Kumasaka, S. Owada, K. Tono, M. Yabashi, Y. Yamaguchi, S. Yanagisawa, M. Sakaguchi, T. Ogura, R. Komiya, J. Yan, E. Yamashita, M. Yamamoto, H. Ago, S. Yoshikawa, T. Tsukihara, A nanosecond time-resolved XFEL analysis of structural changes associated with CO release from cytochrome c oxidase. *Sci. Adv.* **3**, e1603042 (2017).

Science Advances

A nanosecond time-resolved XFEL analysis of structural changes associated with CO release from cytochrome c oxidase

Atsuhiro Shimada, Minoru Kubo, Seiki Baba, Keitaro Yamashita, Kunio Hirata, Go Ueno, Takashi Nomura, Tetsunari Kimura, Kyoko Shinzawa-Itoh, Junpei Baba, Keita Hatano, Yuki Eto, Akari Miyamoto, Hironori Murakami, Takashi Kumasaka, Shigeki Owada, Kensuke Tono, Makina Yabashi, Yoshihiro Yamaguchi, Sachiko Yanagisawa, Miyuki Sakaguchi, Takashi Ogura, Ryo Komiya, Jiwang Yan, Eiki Yamashita, Masaki Yamamoto, Hideo Ago, Shinya Yoshikawa and Tomitake Tsukihara

Sci Adv **3** (7), e1603042.
DOI: 10.1126/sciadv.1603042